Low-loss SiGe waveguides for mid-infrared photonics fabricated on 200 mm wafers

Victor Turpaud, Thi Hao Nhi Nguyen, Hamza Dely, Natnicha Koompai, Annabelle Bricout, Jean-Michel Hartmann, Nicolas Bernier, Julia Krawczyk, Gabriel Lima, Samson Edmond, et al.

Research Article | Vol. 32, No. 10 / 6 May 2024 / Optics Express 17400

Optics EXPRESS

Low-loss SiGe waveguides for mid-infrared photonics fabricated on 200 mm wafers

VICTOR TURPAUD,[1,*] THI-HAO-NHI NGUYEN,[1] HAMZA DELY,[1] NATNICHA KOOMPAI,[1] ANNABELLE BRICOUT,[1] JEAN-MICHEL HARTMANN,[2] NICOLAS BERNIER,[2] JULIA KRAWCZYK,[2] GABRIEL LIMA,[2] SAMSON EDMOND,[1] ETIENNE HERTH,[1] CARLOS ALONSO-RAMOS,[1] LAURENT VIVIEN,[1] AND DELPHINE MARRIS-MORINI[1]

[1] *Centre de Nanosciences et de Nanotechnologies, CNRS, Universite Paris-Saclay, Palaiseau, 91120, France*
[2] *Universite Grenoble-Alpes, CEA-LETI, Grenoble, 38054, France*
[*] *victor.turpaud@universite-paris-saclay.fr*

Abstract: This article presents low-loss mid-infrared waveguides fabricated on a Ge-rich SiGe strain-relaxed buffer grown on an industrial-scale 200 mm wafer, with propagation losses below 0.5 dB/cm for 5-7 µm wavelengths and below 5 dB/cm up to 11 µm. Investigation reveals free-carrier absorption as the primary loss factor for 5-6.5 µm and silicon multiphonon absorption beyond 7 µm wavelength. This result establishes a foundation for a scalable, silicon-compatible mid-infrared platform, enabling the realisation of photonic integrated circuits for various applications in the mid-infrared spectral region, from hazard detection to spectroscopy and military imaging.

1. Introduction

Mid-infrared integrated photonics has recently attracted a lot of attention due to the wide range of key applications it can address, such as hazard detection [1], free-space data transmission in the mid-infrared transparency windows of the atmosphere [2], spectroscopy [3–5], astrophotonics [6] or military imaging. Obtaining such functionalities on-chip requires an integrated platform, and several candidates already exist, such as silicon [7,8], III-V materials benefiting from monolithic integration capabilities [9], silicon-on-sapphire [10] or chalcogenides [11]. However, to benefit from CMOS-compatible processes, many platforms using germanium and silicon [12,13] have also been proposed, such as suspended germanium [14], germanium on silicon [15–17], SiGe on silicon [18], and Ge-rich graded SiGe [19,20]. The latter enables to confine the optical mode away from the silicon substrate, which is known to absorb above 7 µm wavelength, and benefits from progresses made in the growth of SiGe alloys for quantum electronics applications [21]. A whole library of photonic integrated circuits components has been developed, such as spectrometers [22], resonators [23], modulators and photodetectors [24–27]. In this paper we investigate for the first time the optical properties of mid-infrared graded SiGe photonic circuits grown on industrial-scale 200 mm wafers. To this end, waveguides with low propagation losses in the 5 to 11 µm wavelength range are fabricated, allowing broadband operation with losses that are compatible with many applications. An extensive study of the origins of propagation losses in this platform is then conducted, in order to further improve its performances in the long-wave infrared.

#521925 https://doi.org/10.1364/OE.521925
Journal © 2024 Received 20 Feb 2024; revised 28 Mar 2024; accepted 16 Apr 2024; published 26 Apr 2024

Optics EXPRESS

2. Sample fabrication

2.1. Presentation of the graded SiGe photonics platform

The platform used consists in a 8 µm thick graded SiGe layer in which the concentration of germanium (Ge) increases linearly, at an approximate rate of 10 % Ge / µm, from 4 up to 79 % Ge in the alloy, followed by a 3 µm thick $Si_{0.21}Ge_{0.79}$ cap. These SiGe layers are grown at 850°C on a 200 mm Si⟨001⟩ substrate in an Epi Centura 5200 epitaxy cluster tool, as described in [21]. A chemical-mechanical polishing process has then been performed, resulting in a final thickness of the cap layer of 2.5 µm. A scanning transmission electron microscope (STEM) image of the whole graded buffer is shown in Fig. 1(a), together with the targeted linear increase of the germanium concentration as a function of the position in the buffer in Fig. 1(b). Energy-dispersive X-ray spectroscopy (EDX) performed in the STEM showed that such a linear increase of the germanium concentration was indeed a very good approximation. The actual EDX profile can be found in [21], together with the estimated value of the threading dislocation density in the constant composition layer of a few 10^5 cm^{-2}.

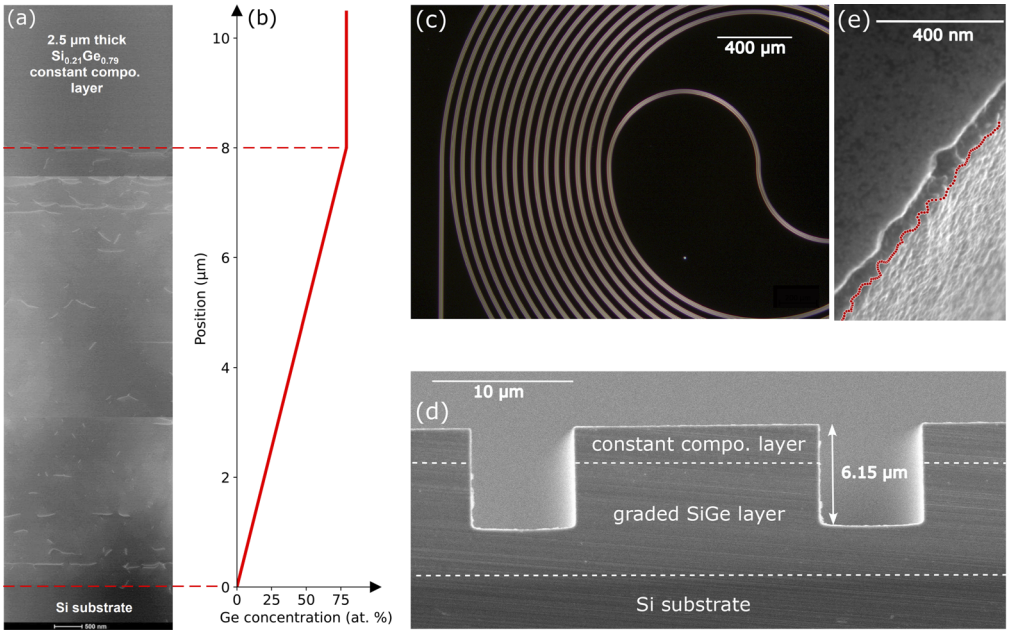

Fig. 1. Platform used to fabricate low-loss SiGe waveguides. **(a)** Stacked dark-field scanning transmission electron microscope (STEM) images showing the whole graded buffer and the cap layer of the platform used. The stacking of different micrographs is responsible for the apparent horizontal lines. Misfit dislocations are confined in the graded buffer, with none seen in STEM in the relaxed 2.5 µm thick cap layer. **(b)** Analytical approximation of the germanium concentration at each position of the graded buffer. **(c)** Dark-field optical microscopy view of part of one of the spirals used to measure propagation losses. **(d)** Scanning electron microscope view of the waveguide facet, showing a 15 µm wide input waveguide used for light coupling. Back-scattered electrons are responsible for the intensity variation as the germanium concentration increases. **(e)** Zoom on a waveguide sidewall used to estimate the sidewall roughness.

Optics EXPRESS

2.2. Waveguides fabrication

In order to measure the propagation losses of optical waveguides fabricated on such a platform, a set of 10 different lengths spiral waveguides varying from 11 mm to 141 mm were fabricated. A dark-field top-view optical microscope image of part of such a spiral is shown in Fig. 1(c). The fabrication process consisted in an electron-beam lithography step to define the future waveguides, followed by an inductively-coupled plasma, reactive-ion etching step using a (SF_6, C_4H_8) chemistry. A continuous etching process yielded straight sidewalls, as shown in Figure 1(d), a scanning electron microscope (SEM) image of a facet. The signal intensity variation is partly coming from back-scattered electrons (BSE), indicating a composition variation towards more germanium in line with Fig. 1(b), as germanium back-scatters more electrons than silicon. These facets, necessary to couple light in and out of the waveguides are produced thanks to optical quality dicing. As visible on Fig. 1(d), the coupling waveguide is 15 µm wide to ensure a better mode-matching at coupling and collection steps. It is then adiabatically shrinked, over a 200 µm propagation distance, into a 5.75 µm-wide waveguide. Such waveguide dimensions ensure that optical modes are guided over the broad wavelength range we are aiming for. A relatively small sidewall roughness, whose RMS value is estimated around 9.5 nm, is obtained, as shown in Fig. 1(e). On the output side, the waveguide is tapered following the same procedure as on the input side, so that waveguides are symmetric.

3. Experimental results

3.1. Experimental setup

Propagation losses are extracted from a standard "cut-back" measurement. To perform such an experiment, 4 quantum cascade lasers (QCL) chips in an external cavity (MIRCAT system, Daylight Solutions) operating in pulsed regime (100 kHz repetition rate, 500 ns pulse width) from 5.08 µm up to 11.21 µm are used as light sources. The light emitted from this system is coupled into the fabricated set of spiral waveguides previously described using a ZnSe aspheric lens, and collected at the output using a similar one. In order to ensure the correct coupling into the waveguides, the collected light is monitored using a mode profiler (WinCamD IR-BB, DataRay or A6750, FLIR). The collected signal intensity is measured using a Nitrogen-cooled HgCdTe photodetector (DSS-MCT-020, Horiba), and its output sent to a lock-in amplifier (SR 810, Stanford Research Systems), synchronised at the pulsed laser repetition rate. This synchronous detection enables to get rid of any noise coming from ambient black-body radiation and thus increases the signal-to-noise ratio. A schematic view of the experimental setup is given in Fig. 2(a), together with an image taken on the mode profiler of the collected TE mode at the output of a 6.6 cm-long waveguide in Fig. 2(b).

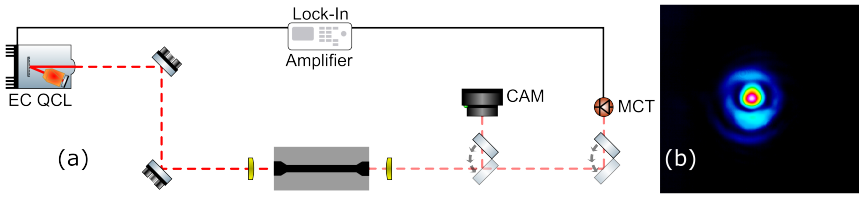

Fig. 2. **(a)** Experimental setup used for propagation losses measurement. An external cavity QCL (**EC QCL**) operating in pulsed regime is used to both synchronise a lock-in amplifier and couple into the SiGe chip. The output is either observed using a mode profiler (**CAM**) or sent to an HgCdTe detector (**MCT**) that is synchronised with the EC QCL. **(b)** Picture taken with the WinCamD IR-BB mode profiler of the collected light from the waveguide at 7.8 µm wavelength, showing single-mode operation of the waveguides.

Optics EXPRESS

3.2. Propagation losses measurements

For each of the four different QCLs in the laser system, the emitted light is coupled into a waveguide of a given length, and the output signal is then collected to be sent, once the correct coupling is ensured using the mode profiler, to the HgCdTe detector to measure the output normalised power. Input and output alignments are performed for each of the QCL at the centre position of its gain spectrum, and the intensity of the output signal is then measured while the input wavelength is swept over the output spectrum of the given QCL. This measurement is done for each QCL and measurable length of waveguide. For the first QCL, emitting between 5.08 µm and 6.02 µm, the acquired transmission spectra for 5 of the measured waveguides in TM polarisation are shown in Fig. 3(a). In order to reduce the intensity oscillations, a 5 points moving average has been performed on such intensity spectra. For each of the resulting wavelengths, as emphasised with the black dashed line in Fig. 3(a), a linear regression of the values of the signal versus the corresponding length of the waveguide is performed, shown in Fig. 3(b). Each slope of the fit then gives rise to a loss value at the given wavelength, represented in red in Fig. 3(c). From such a fit, 95 % confidence intervals are inferred using the standard error of the fit, normalised by the quantile function of a Student's t-distibution, assuming that data-points follow such a distribution around their actual slope. These 95 % confidence intervals are shown in blue on Fig. 3(c). It is worth noting that data shown in Fig. 3 are processed using only 5 different lengths and the TM polarisation only for clarity purposes. However, actual data processing is performed using all the measurable lengths for each of the QCLs and both TE and TM polarisations. These propagation losses measurements are performed for each of the four QCLs and concatenated together. For some points, an overlap between two different QCLs exists. Data giving the smallest

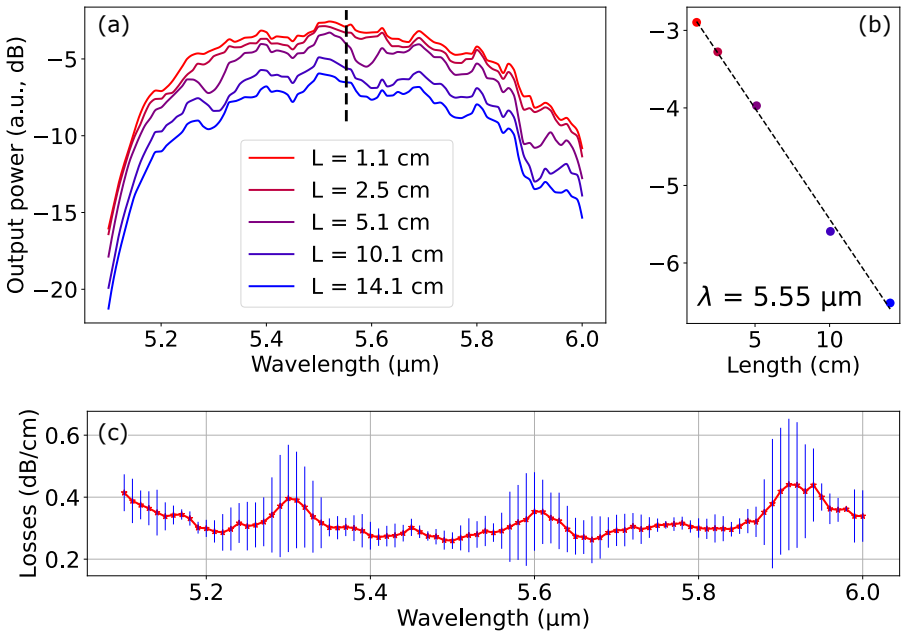

Fig. 3. Example of propagation losses extraction for the various wavelengths accessible by each QCL chip. **(a)** Measurement of the output power in TM polarisation as a function of the wavelength for different waveguides lengths, once the 5 points moving average window has been applied. **(b)** Linear fit for the losses extraction at 5.55 µm wavelength, corresponding to the dashed line in Fig. 3(a). **(c)** Resulting propagation losses using the linear fit for each of the wavelength in red, with the corresponding 95 % confidence bounds in blue.

Optics EXPRESS

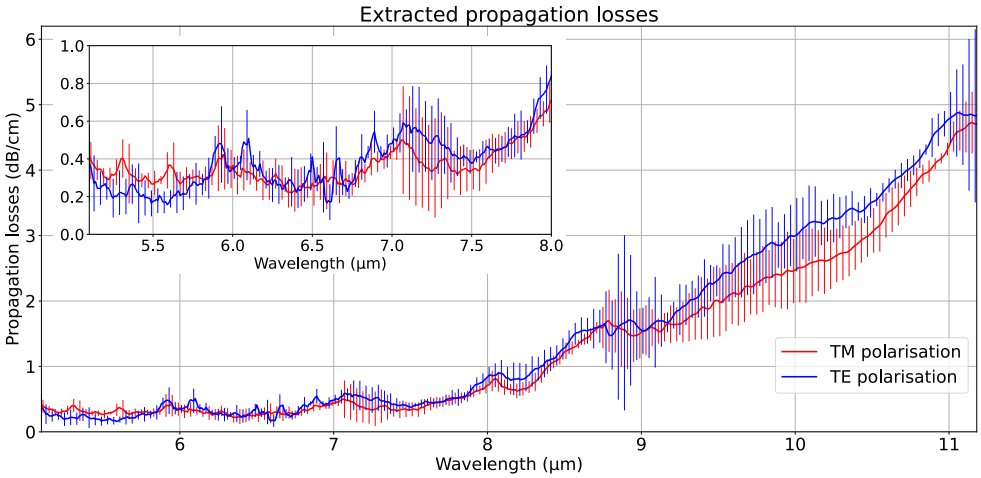

Fig. 4. Propagation losses from cut-back measurements. Thick lines yield the estimated propagation losses, while the thin vertical lines correspond to the 95 % confidence interval. **Inset:** Zoom on the wavelengths below 8 µm to emphasise the low propagation losses in this spectral region.

uncertainty on propagation losses are then used. The resulting propagation losses curve on the entire wavelength range accessible with our laser system is shown in Fig. 4. These propagation losses are lower than 0.5 dB/cm up to 7 µm wavelength and between 0.5 and 1 dB/cm from 7 up to 8 µm wavelength. They stay below 5 dB/cm over the entire operation bandwidth.

4. Physical origins of the losses

Models accounting for sidewall roughness, free carrier absorption and multiphonon absorption were used to account for propagation losses in our SiGe waveguides. This study has been performed under the assumption of single mode propagation. Although fabricated waveguides allow multimode operation in the lower wavelengths range, no clear multimode operation was observed using the mode profiler, confirming the validity of this assumption. Those contributions to propagation losses are summarised in Fig. 5.

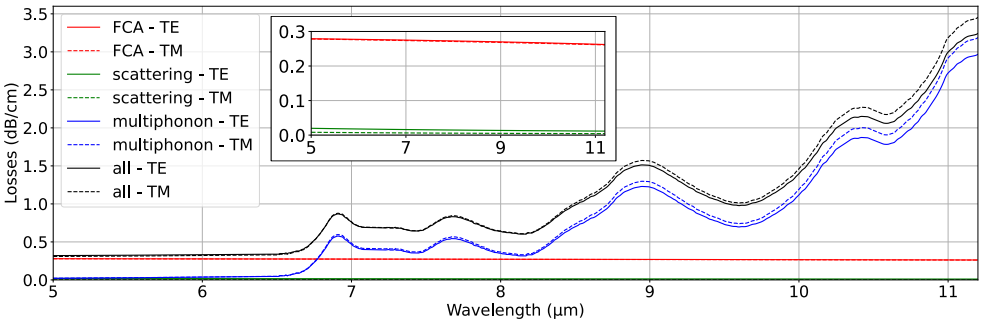

Fig. 5. Simulated propagation losses using the described model. Each contribution to losses described in the model is shown individually. FCA: free-carrier absorption. Scattering: losses due to scattering from sidewalls, which are nearly negligible. Multiphonon: multiphonon absorption of silicon. All: Sum of all the aforementioned contributions. **Inset:** Zoom on the contribution of FCA and scattering from sidewall roughness.

Optics EXPRESS

4.1. Sidewall roughness losses

Scattered light from the optical mode contributes to propagation losses. Since chemical-mechanical polishing has been performed on the top layer, scattering from the top of the waveguide is negligible. Scattering losses originating from the transition between the silicon wafer and the graded buffer is also neglected. Only scattering losses coming from sidewall roughness are thus taken into account. A theoretical model of radiation losses due to sidewall roughness [28] has already been established. It is used here in order to evaluate the contribution of sidewall roughness to propagation losses. Losses are given by:

$$\alpha = \varphi^2(d)\left(n_1^2 - n_2^2\right)^2 \frac{k_0^3}{4\pi n_1} \int_0^{\pi} \tilde{R}\left(\beta - n_2 k_0 cos(\theta)\right) d\theta \tag{1}$$

where φ^2 is the normalised intensity distribution over the lateral dimension, d is the half-width of the waveguide, n_1 and n_2 are respectively the core and cladding refractive indices, β and k_0 the mode and vacuum propagation constants. $\tilde{R}$ is the Fourier transform of the sidewall roughness auto-correlation function, and the right $S = \int_0^{\pi} \tilde{R}\left(\beta - n_2 k_0 cos(\theta)\right) d\theta$ integral of Eq. (1) describes the sum of the powers carried by each scattered plane-wave at each angle, following the roughness spatial-frequency distribution [29]. β and $\varphi^2(d)$ are computed using a mode solver, using the indices of Si and Ge [30], with linear interpolations performed to deduce the real part of the index of any SiGe alloy from pure Si to pure Ge. In order to obtain the roughness auto-correlation function R, slightly tilted top view scanning electron microscope images of a sidewall were captured. A line following the top of the sidewall was drawn as shown on Fig. 1(e) and the lateral dimension corrected by the tilt used to correctly image the top of the sidewall. The auto-correlation of this measurement is calculated, and a Gaussian fit $R(u) = \sigma_{RMS}^2 \exp\left(\frac{-u^2}{L_c^2}\right)$ performed to deduce a coherence length L_c and a root mean square roughness σ_{RMS} of sidewall imperfections. The obtained values $\sigma_{RMS} = 9.5$ nm and $L_c = 19$ nm are in good agreement with previously reported values [20]. These values enable to compute the S integral and determine losses. These losses are, as to be expected from Rayleigh scattering theory, low at these mid-infrared wavelengths, as they scale with λ^{-4} [31]. The contribution of scattering losses remains below 0.02 dB/cm over the entire wavelength range, as shown in the inset of Fig. 5.

4.2. Free-carriers absorption

The next physical phenomenon at the origin of propagation losses is free-carrier absorption (FCA). In order to model the influence of such free-carriers on losses, established models of FCA in silicon [32] and germanium [33] were used. A linear fit between pure Si and pure Ge parameters has been performed to determine the FCA of a given SiGe alloy. The mode solver used to compute sidewall roughness losses is used at the same time to determine an effective FCA from the overlap between the power distribution in the mode and the different germanium concentrations in the waveguide. In order to estimate the residual non-intentional doping type and concentration in the waveguide, a set of square mesa electrical contacts have been fabricated to perform C-V measurements. The dopant concentration could then be evaluated [34]. A residual P-type dopant concentration around 10^{14}-10^{15} cm^{-3} in the graded buffer and top layer was estimated from such C-V measurements. A finer estimation of the residual doping could be extracted from propagation losses in the shortest wavelengths, indicating that this residual dopant concentration is actually close to 2×10^{14} cm^{-3}. This finer estimation is indeed reasonable as FCA represent the dominant source of losses in this spectral region [15,20], as shown in Fig. 5. It is also worth noting that this value is below the lower bound of 2×10^{15} cm^{-3} given in [33], but a good estimation outside of these bounds could still apparently be extracted [15]. Finally, it can be noted that the FCA contribution appears to be nearly wavelength-independent, which can

Optics EXPRESS

be counterintuitive as FCA increases with the wavelength in both Si and Ge [32,33]. However, this is explained by the mode confinement variation with the wavelength. Indeed, FCA is smaller for Si than Ge, and as the wavelength increases, the overlap with silicon-rich sections increases, thus compensating for the increasing FCA in bulk Si or Ge.

4.3. Silicon multiphonon absorption

Another source of propagation losses in the system is silicon multiphonon absorption in both the silicon wafer and the the SiGe alloy. The experimental absorption of pure silicon is provided in several Refs. [35,36]. However, no detailed study of infrared absorption in the mid-infrared that would lead to an estimation of multiphonon absorption in SiGe alloys exists to the best of our knowledge in the literature. An estimation of multiphonon absorption in the long-wave infrared has thus been performed in our waveguides. This estimation enables to conclude on whether this absorption is the major contribution to losses in the long-wave infrared observed in Fig. 4. To perform such an estimation, the multiphonon absorption of germanium was considered to be negligible in the wavelength range probed compared to that of silicon. The values of high-resistivity silicon absorption provided in [35] was considered to be mainly coming from multiphonon absorption, and taken to recover the imaginary part of the refractive index. It has been completed by values measured in [36] for wavelengths below 6.4 μm. For each $Si_{1-x}Ge_x$ alloy, the multiphonon absorption of silicon has been rescaled by a $(1-x)$ factor, and the effective multiphonon absorption estimated by calculating the effective losses from the mode overlap between each germanium concentration in the waveguide and the optical intensity in the mode. The estimated propagation losses coming from the presence of silicon in the alloy is shown in blue in Fig. 5. It should be noted that this normalisation of multiphonon absorption in SiGe alloys by the Ge concentration does not rely on a proper modeling, and a deeper analysis would help refining the model. However, a reasonable agreement with the experimental measurements is obtained.

4.4. Analysis

The model created here to simulate the propagation losses, defined as the sum of all the studied contributions and shown in black on Fig. 5, gives a fairly good estimation in the 5 to 9 μm range. However, a difference below 2 dB/cm between the theoretical model and the experimental measurements is observed above 9 μm wavelength. Several phenomena detailed hereafter could explain this difference. One first possible source of discrepancy between experiments and modeling that has not been accounted for in the precedent model is the residual strain in the graded buffer, that modifies the dispersion relation of phonons in the crystalline structure and thus the multiphonon absorption. However, to our knowledge, no studies have been performed on the relationship between multiphonon absorption and strain in SiGe alloys. Another possible origin of this deviation is the presence of dislocations in the graded SiGe layer, as shown in Fig. 1(a), which can contribute more to absorption at large wavelengths, since the optical mode size increases, and so does the overlap between this mode and these dislocations. It is however hard to precisely quantify the relation between the dislocation density and propagation losses.

5. Conclusion and perspectives

We have fabricated Ge-rich SiGe optical waveguides that cover the whole 5 to 11 μm wavelength range. In the 5 to 7 μm range, losses below 0.5 dB/cm are demonstrated. These losses stay below 1 dB/cm up to 8 μm, and below 5 dB/cm over the entire measured wavelength range. By analysing the different contributions to these propagation losses, it is shown that they are mainly FCA-limited from 5 to 6.5 μm. Losses could be further reduced by reducing residual p-type dopant concentration to values below 2×10^{14} cm^{-3}, which could be hard. A switching over to n-type or no doping using dopant compensation techniques, since n-type doping is expected

Optics EXPRESS

to produce lower propagation losses in both silicon and germanium [32,33], could also help. This analysis also shows that silicon multiphonon absorption remains the limiting factor above 7 μm wavelength, paving the way for further improvements. Increasing the germanium final concentration to pure germanium, centring the mode in it and thus staying far from high-Si concentration regions of the graded buffer would address this issue. Increasing the thickness of the graded buffer also allows to reduce silicon multiphonon absorption, as the overlap of the mode with silicon-rich sections reduces. This is shown by the lower losses obtained beyond 10 μm in [20], where an 11 μm thick graded buffer has been used. This low losses silicon-compatible mid-infrared platform grown with industrial epitaxy tools would allow a wide range of applications, ranging from high quality-factor resonators [23] in the mid-infrared spectral region, to optical delay-lines or energy-efficient nonlinear integrated photonics [37–40].

Funding. RENATECH; European Research Council (ERC-Electrophot, 101097569); Conseil Départemental de l'Essonne.

Acknowledgments. The fabrication of the device was partially performed at the Plateforme de MicroNanotechnologies/C2N, which is partially funded by the "Conseil général de l'Essonne". This work was partly supported by the French RENATECH network. CEA-LETI is acknowledged for the SiGe epitaxial growth. Co-funded by the European Union (ERC-Electrophot, 101097569). Views and opinions expressed are however those of the authors only and do not necessarily reflect those of the European Union or the European Research Council. Neither the European Union nor the granting authority can be held responsible for them.

Disclosures. The authors declare no conflicts of interest.

Data availability. The data that support the findings of this study are openly available at Zenodo repository [41].

References

1. T. Jin, H.-Y. G. Lin, T. Tiwald, *et al.*, "Flexible mid-infrared photonic circuits for real-time and label-free hydroxyl compound detection," Sci. Rep. **9**(1), 4153 (2019).
2. H. Dely, T. Bonazzi, and O. Spitz, "10 Gbit s-1 free space data transmission at 9 μm wavelength with unipolar quantum optoelectronics," Laser Photonics Rev. **16**(2), 2100414 (2022).
3. N. Picqué and T. W. Hänsch, "Frequency comb spectroscopy," Nat. Photonics **13**(3), 146–157 (2019).
4. M. Yu, Y. Okawachi, and A. G. Griffith, "Silicon-chip-based mid-infrared dual-comb spectroscopy," Nat. Commun. **9**(1), 1869 (2018).
5. G. Scalari, J. Faist, and N. Picqué, "On-chip mid-infrared and THz frequency combs for spectroscopy," Appl. Phys. Lett. **114**(15), 150401 (2019).
6. N. Jovanovic, P. Gatkine, N. Anugu, *et al.*, "2023 astrophotonics roadmap: pathways to realizing multi-functional integrated astrophotonic instruments," J. Phys. Photonics **5**, 042501 (2023).
7. H. Lin, Z. Luo, and T. Gu, "Mid-infrared integrated photonics on silicon: A perspective," Nanophotonics **7**(2), 393–420 (2017).
8. J. S. Penadés, C. Alonso-Ramos, and A. Z. Khokhar, "Suspended SOI waveguide with sub-wavelength grating cladding for mid-infrared," Opt. Lett. **39**(19), 5661–5664 (2014).
9. S. Jung, D. Palaferri, and K. Zhang, "Homogeneous photonic integration of mid-infrared quantum cascade lasers with low-loss passive waveguides on an InP platform," Optica **6**(8), 1023–1030 (2019).
10. F. Li, S. D. Jackson, and C. Grillet, "Low propagation loss silicon-on-sapphire waveguides for the mid-infrared," Opt. Express **19**(16), 15212–15220 (2011).
11. A. Gutierrez-Arroyo, E. Baudet, and L. Bodiou, "Optical characterization at 7.7 μm of an integrated platform based on chalcogenide waveguides for sensing applications in the mid-infrared," Opt. Express **24**(20), 23109–23117 (2016).
12. R. Soref, "Mid-infrared photonics in silicon and germanium," Nat. Photonics **4**(8), 495–497 (2010).
13. D. Marris-Morini, V. Vakarin, and J. M. Ramirez, "Germanium-based integrated photonics from near- to mid-infrared applications," Nanophotonics **7**(11), 1781–1793 (2018).
14. A. Sánchez-Postigo, A. Ortega-Moñux, and J. S. Penadés, "Suspended germanium waveguides with subwavelength-grating metamaterial cladding for the mid-infrared band," Opt. Express **29**(11), 16867–16878 (2021).
15. M. Nedeljkovic, J. S. Penades, and V. Mittal, "Germanium-on-silicon waveguides operating at mid-infrared wavelengths up to 8.5 μm," Opt. Express **25**(22), 27431–27441 (2017).
16. Y.-C. Chang, V. Paeder, and L. Hvozdara, "Low-loss germanium strip waveguides on silicon for the mid-infrared," Opt. Lett. **37**(14), 2883–2885 (2012).
17. K. Gallacher, R. W. Millar, and U. Griškevičiūte, "Low loss Ge-on-Si waveguides operating in the 8–14 μm atmospheric transmission window," Opt. Express **26**(20), 25667–25675 (2018).
18. C. Grillet, P. Ma, B. Luther-Davies, *et al.*, "Low loss SiGe waveguides in the MID-IR," in *2013 Conference on Lasers & Electro-Optics Europe & International Quantum Electronics Conference CLEO EUROPE/IQEC*, (2013), pp. 1–1.
19. J. M. Ramirez, V. Vakarin, and C. Gilles, "Low-loss Ge-rich $Si_{0.2}Ge_{0.8}$ waveguides for mid-infrared photonics," Opt. Lett. **42**(1), 105–108 (2017).

Optics EXPRESS

20. M. Montesinos-Ballester, V. Vakarin, and Q. Liu, "Ge-rich graded SiGe waveguides and interferometers from 5 to 11 μm wavelength range," Opt. Express **28**(9), 12771–12779 (2020).
21. J.-M. Hartmann, N. Bernier, and F. Pierre, "Epitaxy of Group-IV semiconductors for quantum electronics," ECS Trans. **111**(1), 53–72 (2023).
22. M. Montesinos-Ballester, Q. Liu, and V. Vakarin, "On-chip Fourier-transform spectrometer based on spatial heterodyning tuned by thermo-optic effect," Sci. Rep. **9**(1), 14633 (2019).
23. N. Koompai, T. H. N. Nguyen, and V. Turpaud, "Long-wave infrared integrated resonators in the 7.5–9 μm wavelength range," Appl. Phys. Lett. **123**(3), 031109 (2023).
24. M. Montesinos-Ballester, L. Deniel, and N. Koompai, "Mid-infrared integrated electro-optic modulator operating up to 225 MHz between 6.4 and 10.7 μm wavelength," ACS Photonics **9**(1), 249–255 (2022).
25. T. H. N. Nguyen, N. Koompai, and V. Turpaud, "1 GHz electro-optical silicon-germanium modulator in the 5-9 μm wavelength range," Opt. Express **30**(26), 47093–47102 (2022).
26. T. H. N. Nguyen, N. Koompai, and V. Turpaud, "Room temperature-integrated photodetector between 5 μm and 8 μm wavelength," Adv. Photonics Res. **4**(2), 2200237 (2023).
27. T. H. N. Nguyen, V. Turpaud, N. Koompai, *et al.*, "Integrated PIN modulator and photodetector operating in the mid-infrared range from 5.5 μm to 10 μm," Nanophotonics (2024).
28. F. P. Payne and J. P. R. Lacey, "A theoretical analysis of scattering loss from planar optical waveguides," Opt. Quantum Electron. **26**(10), 977–986 (1994).
29. J. P. R. Lacey and F. P. Payne, "Radiation loss from planar waveguides with random wall imperfections," IEE Proc. J Optoelectron. UK **137**(4), 282–289 (1990).
30. H. H. Li, "Refractive index of silicon and germanium and its wavelength and temperature derivatives," J. Phys. Chem. Ref. Data **9**(3), 561–658 (1980).
31. K. K. Lee, D. R. Lim, and H.-C. Luan, "Effect of size and roughness on light transmission in a Si/SiO_2 waveguide: Experiments and model," Appl. Phys. Lett. **77**(11), 1617–1619 (2000).
32. M. Nedeljkovic, R. Soref, and G. Z. Mashanovich, "Free-carrier electrorefraction and electroabsorption modulation predictions for silicon over the 1–14-μm infrared wavelength range," IEEE Photonics J. **3**(6), 1171–1180 (2011).
33. M. Nedeljkovic, R. Soref, and G. Z. Mashanovich, "Predictions of free-carrier electroabsorption and electrorefraction in germanium," IEEE Photonics J. **7**(3), 1–14 (2015).
34. S. M. Sze, *Physics of Semiconductor Devices* (Wiley -Interscience, 1969), international edition ed.
35. D. Chandler-Horowitz and P. M. Amirtharaj, "High-accuracy, midinfrared (450 $cm^{-1} \leq \omega \leq 4000\ cm^{-1}$) refractive index values of silicon," J. Appl. Phys. **97**(12), 1 (2005).
36. E. Shkondin, O. Takayama, and M. E. A. Panah, "Large-scale high aspect ratio Al-doped ZnO nanopillars arrays as anisotropic metamaterials," Opt. Mater. Express **7**(5), 1606–1627 (2017).
37. D. Kazakov, T. P. Letsou, and M. Beiser, "Active mid-infrared ring resonators," Nat. Commun. **15**(1), 607 (2024).
38. M. Montesinos-Ballester, C. Lafforgue, and J. Frigerio, "On-chip mid-infrared supercontinuum generation from 3 to 13 μm wavelength," ACS Photonics **7**(12), 3423–3429 (2020).
39. J. M. Ramirez, V. Vakarin, and J. Frigerio, "Ge-rich graded-index Si_{1-x}Gex waveguides with broadband tight mode confinement and flat anomalous dispersion for nonlinear mid-infrared photonics," Opt. Express **25**(6), 6561–6567 (2017).
40. V. Turpaud, N. Koompai, T. H. Nhi Nguyen, *et al.*, "Enhancing mid-infrared supercontinuum generation at low pump power in SiGe waveguides," in *2023 Conference on Lasers and Electro-Optics Europe & European Quantum Electronics Conference (CLEO/Europe-EQEC)*, (2023), pp. 1–1.
41. V. Turpaud, T. H. Nhi Nguyen, D. Hamza, *et al.*, "Dataset for Low-loss SiGe waveguides for mid-infrared photonics fabricated on 200 mm wafers," Zenodo (2023) https://doi.org/10.5281/zenodo.11062163.